New Journal of Physics
The open-access journal for physics

Carbon ion acceleration from thin foil targets irradiated by ultrahigh-contrast, ultraintense laser pulses

D C Carroll[1], O Tresca[1], R Prasad[2], L Romagnani[2], P S Foster[2,3], P Gallegos[1,3], S Ter-Avetisyan[2], J S Green[3], M J V Streeter[3,4], N Dover[4], C A J Palmer[4], C M Brenner[1,3], F H Cameron[3], K E Quinn[2], J Schreiber[4], A P L Robinson[3], T Baeva[3], M N Quinn[1], X H Yuan[1], Z Najmudin[4], M Zepf[2], D Neely[1,3], M Borghesi[2] and P McKenna[1,5]

[1] SUPA Department of Physics, University of Strathclyde, Glasgow G4 0NG, UK
[2] School of Mathematics and Physics, Queen's University Belfast, Belfast BT7 1NN, UK
[3] Central Laser Facility, STFC Rutherford Appleton Laboratory, Didcot, Oxfordshire OX11 0QX, UK
[4] The Blackett Laboratory, Imperial College London, London SW7 2AZ, UK
E-mail: p.mckenna@phys.strath.ac.uk

New Journal of Physics **12** (2010) 045020 (15pp)
Received 13 November 2009
Published 30 April 2010
Online at http://www.njp.org/
doi:10.1088/1367-2630/12/4/045020

Abstract. In this study, ion acceleration from thin planar target foils irradiated by ultrahigh-contrast (10^{10}), ultrashort (50 fs) laser pulses focused to intensities of 7×10^{20} W cm^{-2} is investigated experimentally. Target normal sheath acceleration (TNSA) is found to be the dominant ion acceleration mechanism when the target thickness is $\geqslant$50 nm and laser pulses are linearly polarized. Under these conditions, irradiation at normal incidence is found to produce higher energy ions than oblique incidence at 35° with respect to the target normal. Simulations using one-dimensional (1D) boosted and 2D particle-in-cell codes support the result, showing increased energy coupling efficiency to fast electrons for normal incidence. The effects of target composition and thickness on the acceleration of carbon ions are reported and compared to calculations using analytical models of ion acceleration.

[5] Author to whom any correspondence should be addressed.

Contents

1. Introduction

Acceleration of protons and heavier ions in interactions of intense laser pulses with thin solid targets has received a great deal of experimental and theoretical interest since multi-MeV-energy ions were first demonstrated in 2000 [1–4]. Laser-generated ion beams have been shown to have a number of desirable properties, including high brightness (up to 10^{13} ions in a picosecond bunch at the source) and low transverse and longitudinal emittance (about 100-fold better than beams produced from typical RF accelerators) [5]. The interest in laser-accelerated ions is driven by the potential compactness and lower cost of these sources compared to more conventional accelerators. Among the many possible applications of laser-generated high-energy ion beams are the fast ignition approach to inertial confinement fusion [6], ion beam radiography [7], nuclear physics [8, 9] and therapeutic medicine [10–13]. The need to optimize and control this novel source of high-energy ions for applications is motivating a worldwide research effort on high-power laser-driven ion acceleration.

Recent work in this area involves the development of techniques to produce ultrahigh-contrast laser pulses, thus enabling the acceleration from ultrathin foil targets to be investigated [14–17]. It has been shown that ions can be efficiently accelerated from targets with thickness in tens of nanometres scale, using ultrashort (30–60 fs) laser pulses with energies of the order of 1 J and peak intensities of $1\text{–}5 \times 10^{19}$ W cm^{-2} [14, 15]. Ion acceleration from the rear surface of the target is attributed to the target normal sheath acceleration (TNSA) mechanism in this intensity regime. Under these conditions, protons with maximum energy up to ~5–6 MeV have been measured. Generally, the maximum ion energy increases with decreasing target thickness. However, there is a lower limit to the target thickness for which the TNSA mechanism works. Low-intensity prepulses and nanosecond-duration amplified spontaneous emission (ASE) can launch shock waves into the target, destroying its integrity or changing the properties of the beam of accelerated protons [18,19]. The levels of the ASE pedestal and any prepulses effectively define the optimum target thickness and maximum ion energy obtained [19]. Ultrahigh-contrast laser pulses enable ion acceleration from ultrathin targets to be investigated. Henig *et al* [16] have demonstrated enhanced laser-driven ion acceleration from targets that are sufficiently thin that laser energy is transmitted through the target via relativistic

transparency [20]. Furthermore, recent numerical simulations and experiments with ultrathin targets suggest transitions to new acceleration regimes with more favourable energy scaling and a more peaked energy spectrum. These include the 'laser breakout afterburner' regime [21], the 'directed Coulomb explosion' regime [10] and the 'radiation pressure acceleration (RPA)' regime [17], [22–29]. The ultrahigh intensities ($>10^{21}\,\mathrm{W\,cm^{-2}}$) required to access these new acceleration mechanisms are at the upper limit of what are achievable with present-day state-of-the-art laser systems.

In this paper, we report on an experimental investigation of carbon ion acceleration by the TNSA mechanism using one of the currently available highest power (115 TW), ultrahigh-contrast (10^{10}), ultrashort pulse (50 fs) laser systems, operating at average intensities of $7 \times 10^{20}\,\mathrm{W\,cm^{-2}}$ (on target). This is an order of magnitude higher intensity than typically achieved in previous ion acceleration experiments with similar laser pulse durations and is comparable to intensities achieved using large-scale picosecond-duration laser systems [30]. We chose to investigate acceleration of carbon ions because of the interest in using laser–plasma acceleration schemes as potential future compact sources for carbon ion therapy. We compared ion acceleration for normal and oblique laser incidence angles and measured the scaling of the maximum and total ion energies with target thickness and composition. The results are discussed with reference to one-dimensional (1D) boosted- and 2D particle-in-cell (PIC) simulations, and calculations using the analytical models introduced by (i) Schreiber *et al* [31] and (ii) Andreev *et al* [32, 33] for ultrahigh-contrast, ultrashort laser irradiation of thin target foils.

2. The experiment

The experiment was performed using the Astra-Gemini laser at the Rutherford Appleton Laboratory. The laser-delivered pulses with duration, τ_L, equal to 50 fs (full-width at half-maximum (FWHM)), with energy, E_L, up to 12 J, at a central wavelength, λ_L, equal to 800 nm. A double plasma mirror system was employed, in which one off-axis parabola (OAP) was used to focus the laser pulses onto the plasma mirrors and a second identical OAP was used to re-collimate the expanding beam, as illustrated schematically in figure 1. Use of the double plasma mirror arrangement enhanced the contrast ratio between the pulse peak intensity and the ASE pedestal intensity by a factor of ~1000. The inherent intensity contrast at 20 ps prior to the peak, for example, was measured, using a third-order scanning autocorrelator, to be $\sim 10^7$. Use of the double plasma mirror system increased this to $\sim 10^{10}$. The overall energy throughput efficiency of the plasma mirrors was 48%, resulting in energies up to 5.8 J on the target. The pulses were focused with an $f/2$ OAP onto the target at one of two fixed incidence angles, θ_L, 0° (along the target normal) and 35° with respect to the target normal. For $\theta_L = 0°$, the radius, r_L, of the laser focal spot was 1.25 μm (the diameter at FWHM was 2.5 μm, containing 35% of the laser energy). The calculated intensity on target was up to $7 \times 10^{20}\,\mathrm{W\,cm^{-2}}$. A $\lambda/4$ waveplate was placed after the plasma mirror system on a limited number of laser shots to enable target irradiation with circularly polarized laser pulses (for $\theta_L = 0°$ only). Unless otherwise stated, the laser pulses were linearly polarized with the electric field vector in the plane of the laser and target normal axes, i.e. p-polarization for $\theta_L = 35°$.

A range of target materials and thicknesses were irradiated to determine the optimum targets for carbon ion acceleration. These include 'uniform' targets of C, C_3H_6 (polypropylene, hereafter referred to as CH), $C_{10}H_{10}O_4$ (mylar, hereafter referred to as CHO), Al and Au (with

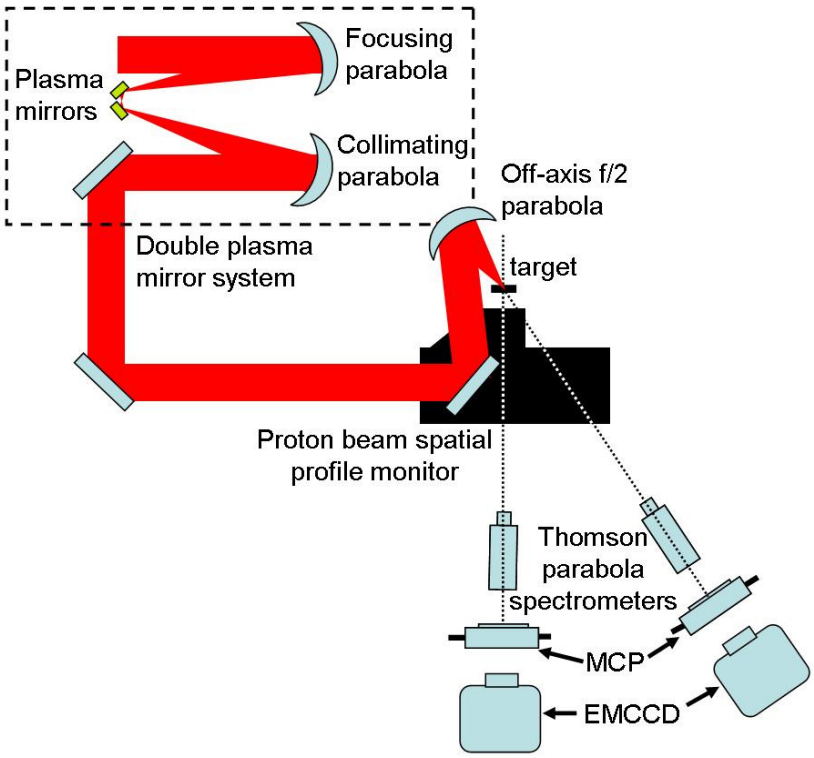

Figure 1. Schematic of the experiment arrangement. A double plasma mirror system was used to enhance the contrast of pulses from the Astra-Gemini laser. The diagnostics included a proton beam spatial intensity profile monitor consisting of plastic scintillators, image relay optics and gated CCD cameras and an identical set of Thomson parabola ion spectrometers with MCP detectors in the dispersion plane and EMCCD cameras.

carbon as a surface contamination layer) and 'layered' Au–CH targets. The target thickness, L, was varied from 10 nm to 10 μm. The target foils were mounted on a rotating wheel to enable a range of different target types to be simultaneously loaded into the target chamber for each parameter scan.

The charge-to-mass ratio and energy distributions of the accelerated ions were measured using two Thomson parabola ion spectrometers, positioned along the target normal direction for each incident angle, as shown in figure 1. They had a line of sight to the laser focal spot in the plane of the laser beam axis and the target normal axis. The dispersed ions were detected using micro-channel plate (MCP) detectors positioned in the dispersion plane of the spectrometers. The output signal from each MCP was measured using an intensified CCD Andor camera (iXon^{EM} + EMCCD 888). The arrangement was absolutely calibrated on a number of laser shots using a CR-39 nuclear track detector, which is sensitive to ions, but insensitive to electrons and x-rays. Slots machined into the CR-39, which was positioned directly in front of the MCP, enabled a direct calibration of the MCP–CCD detector with respect to the CR-39 for the same laser shots. The spatial intensity distribution of the lower half (just below the plane of the spectrometers and the target normal axis) of the proton beam was measured, for protons with energy above a lower detection limit of 5 MeV (defined by the thickness of a

light-shield aluminium filter), using a plastic scintillator and gated CCD imaging system. The aluminium filter stops heavier ions from reaching the scintillator and protects it from the target debris.

3. Ion acceleration mechanisms

As introduced above, for ion acceleration driven by ultrashort laser pulses in the intensity regime from 10^{18} to 10^{20} W cm^{-2}, the TNSA mechanism dominates for targets greater than ~50 nm in thickness [16]. In this scheme, fast electrons ponderomotively accelerated by the laser pulse at the front irradiated surface of the target propagate through the target and exit the rear, setting up a large electrostatic field (of the order of TV m^{-1}) due to the charge separation between the escaping electrons and the ions at the rear surface. The maximum ion energy scales as $I^{1/2}$ and the ion beam is directed along the target normal axis [4]. For higher laser intensities or ultrathin targets, other ion acceleration mechanisms become feasible. If the target thickness is reduced to the order of the relativistic plasma skin depth, then the laser field can penetrate the target to the rear surface, enhancing the TNSA mechanism. This is termed the 'laser break-out afterburner' [16, 34]. The 'Coulomb explosion' (or 'directed Coulomb explosion') mechanism, in which the laser field expels all electrons from the foil, giving rise to an explosion of the ions due to the repulsive Coulomb force between them, becomes important if the target is thin enough (e.g. <100 nm) [35]. The most effective mechanism for coupling laser energy to ions is predicted to be RPA for which the momentum of the laser is efficiently imparted to the ions [17], [22–28]. This mechanism, which can work both for ultrathin targets in 'light-sail' mode [25] and thicker targets in 'hole-boring' mode [26], is predicted to be particularly effective for circularly polarized laser pulses, which gives rise to a non-oscillating electrostatic field and therefore a smooth pushing effect by the radiation pressure of the laser pulse. The RPA mechanism is also feasible in the intensity regime accessed in this experiment, but is likely to become more important at higher intensities. A peaked spectrum of ion energies is predicted, with energy scaling approximately linearly with laser intensity, which is much more favourable than TNSA. The beam would be centred on the direction of propagation of the laser pulse.

To identify the dominant ion acceleration mechanisms in this experiment, we begin by considering the energy spectra of the accelerated ions. Figure 2 shows representative example carbon ion energy spectra from Al targets irradiated with linearly polarized laser pulses focused to average intensity equal to 6–7 $\times$ 10^{20} W cm^{-2}. The spectra were measured along the target normal axis of 100 nm-thick Al targets irradiated at $\theta_L = 35^\circ$ and 0°. Figure 2 is typical of the energy spectral shape obtained for targets with thickness greater than or equal to 100 nm and is consistent with previous measurements of ions accelerated by the TNSA mechanism [3, 36]. The energy distribution shifts to higher energy with increasing charge state, and higher charge state ions exhibit more plateau-like distributions. By contrast, when targets thinner than 50 nm are irradiated, changes to the shape of the spectra at high energy, including the onset of peaks and the detection of ion species with the same maximum velocity, are measured. These spectral changes indicate that TNSA is not the sole mechanism responsible for the ion acceleration in ultrathin (<50 nm) targets and that RPA may start becoming important under these conditions. These observations, which primarily occur with circularly polarized laser pulses and for $\theta_L = 0^\circ$, will be reported in detail in a separate article. In the remainder of the present paper, we focus our attention on carbon ion acceleration by TNSA at ultrahigh laser intensities, using linearly polarized laser pulses.

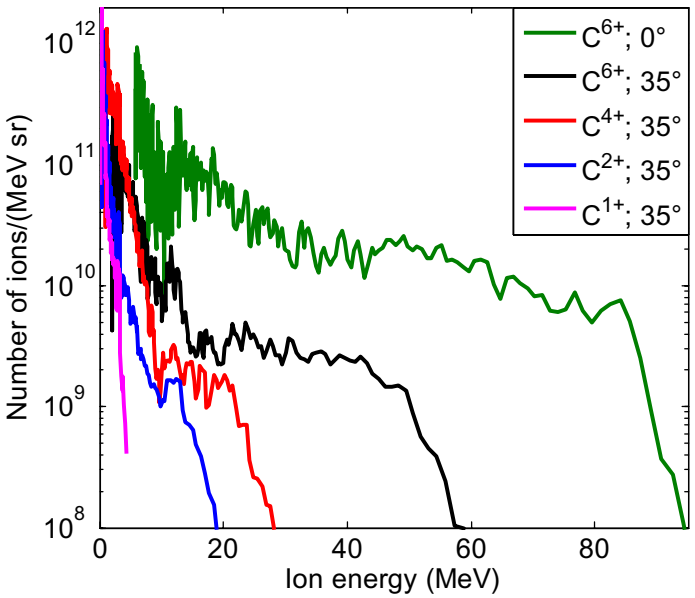

Figure 2. Example carbon ion energy spectra measured along the target normal axis at the rear side of 100 nm-thick Al targets for laser incident angles of 0° and 35° with respect to the target normal axis. The example spectra measured for $\theta_L = 35°$ illustrate the changes with ion charge state. A typical C^{6+} energy spectrum measured for $\theta_L = 0°$ is included to demonstrate the enhancement of ion maximum energy and flux achieved compared to the corresponding spectrum with $\theta_L = 35°$. In both the cases, the laser pulses were linearly polarized, with energy 5 J (on the target), duration 50 fs and intensity 6–7 $\times 10^{20}$ W cm^{-2}.

4. The effect of laser incidence angle

One of the most striking results of this study is the effect of laser incident angle on ion acceleration. As shown in the example spectra in figure 2, the maximum carbon ion energy observed for $\theta_L = 0°$ (equivalent to s-polarized normal incidence) is significantly larger than for 35° (p-polarized) irradiation for otherwise identical laser pulse energy, duration and very similar intensity. As will be shown in figure 4, this observation is correct independent of target thickness. We note that measurements of the spatial intensity distribution of the beam of protons (with energy above a lower detection limit of 5 MeV) show no evidence of changes to the uniformity or beam pointing for the different angles of laser irradiance. Likewise, we do not measure significant changes to the shape of the ion energy spectra, as illustrated in figure 2.

This result contrasts sharply with measurements reported by Ceccotti *et al* [15] on the effect of laser polarization on proton acceleration using ultrahigh-contrast (10^{10}), ultrashort (65 fs) laser pulses focused to 5×10^{18} W cm^{-2}. Those results show that at this lower intensity range the ion energy is enhanced by the p-component of the laser electric field (via, for example, the Brunel effect [37] or the collisionless absorption process suggested by Gibbon [38]). For $\theta_L = 0°$, because the laser electric field is in the plane of the target, the Brunel effect and other p-polarization-dependent absorption mechanisms cannot take place effectively. The fact that much more efficient coupling of laser energy to ions is observed for normal incidence compared to oblique incidence at the higher intensities accessed in the present experiment, which cannot

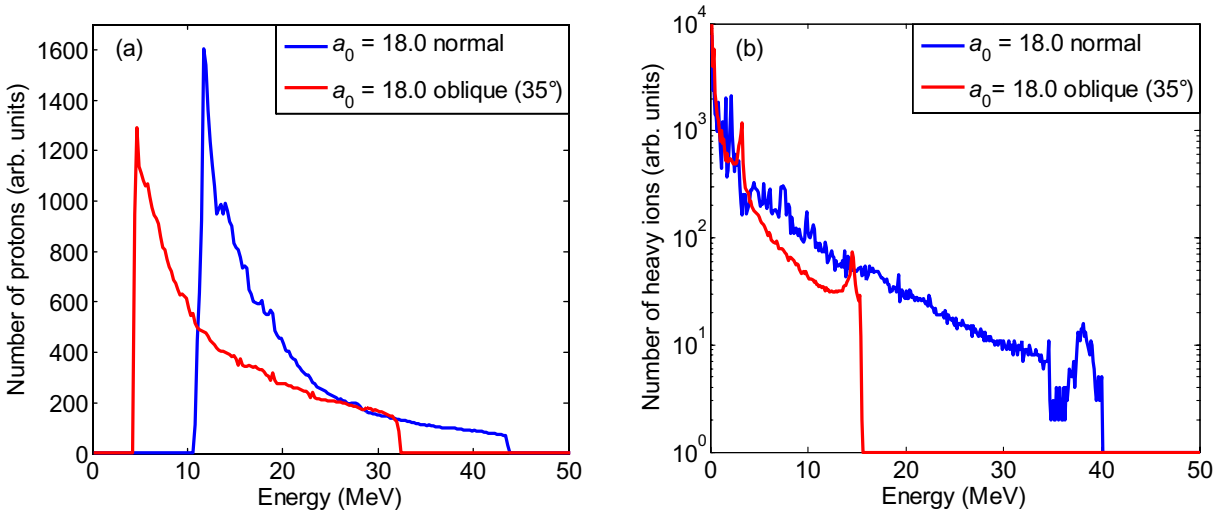

Figure 3. (a) Proton and (b) heavier ion energy spectra from 1D-boosted PIC simulations, showing an enhancement of energy for $\theta_L = 0^\circ$ compared to $\theta_L = 35^\circ$ for otherwise identical laser and target parameters. The spectra are produced at 150 fs after the start of the laser pulse.

be accounted for by the small difference in the ponderomotive potential for the two angles investigated, suggests that new angle-dependent absorption processes may be accessed in the ultrahigh intensity regime for ultrashort laser pulses.

To investigate the possible reasons for the higher energies achieved with $\theta_L = 0^\circ$ compared to $\theta_L = 35^\circ$, 1D-boosted PIC simulations using a modified version of the code employed in [23, 26], [39–41] are performed to investigate any changes in the fast electron generation. The simulations are performed with 25 000 cells, with an individual cell size of 2 nm and 200 particles per cell. The target consists of a heavier ion substrate ($Z = 1$; mass $= 3m_p$, where m_p is the proton mass) at a number density of $90n_c$ where n_c is the critical density, with a 20 nm proton layer (also at $90n_c$) on the rear surface. The acceleration of both ion species is simulated. The laser pulse has a '$\sin^2$' profile with a pulse duration of 50 fs, a wavelength of 0.8 μm and an a_0 (dimensionless amplitude) of 18.0 (equivalent to 7×10^{20} W cm^{-2}). Two simulations are performed, one for a laser incident angle equal to 35° and the other for normal incidence. The simulations reveal that higher-energy ions are produced at normal incidence, as shown in figure 3. The enhancement factors are similar to that measured experimentally for carbon ions (see figure 2). On investigating the simulation output in more detail, it was found that this difference is due to higher energy fast electrons being produced in the normal incidence case than in the oblique incidence case. 2D PIC simulations using the EPOCH code also show a similar effect of the laser-to-fast electron momentum transfer dependence on incident angle. We anticipate that a theoretical description of this new mechanism will be required to fully explain both simulation and experiment. This will be the subject of a detailed investigation in the future.

5. Ion acceleration as a function of target thickness

In this section, we discuss the scaling of the maximum C^{6+} ion energy (the highest energy carbon ion detected) with target thickness. A summary of the measurements using Al, C and

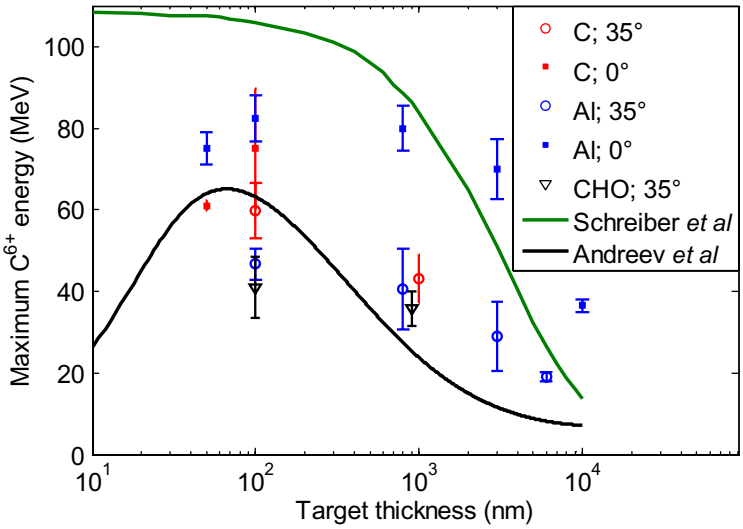

Figure 4. Average of the maximum C^{6+} ion energies measured as a function of target thickness for given target materials and angles of incidence (symbols). Lines correspond to predictions using the analytical models of Andreev *et al* [32] (black line) and Schreiber *et al* [31] (green line), as described in the main text.

CHO target foils, for both angles of incidence, is presented in figure 4. Each point corresponds to an average of the maximum C^{6+} ion energies obtained from a number of laser shots (typically 3 or 4) on each target type and thickness and the error bars correspond to the standard deviation of the maximum energies. While we have chosen here to plot averages of short series of shots for nominally the same conditions, a discussion of the highest ion energies observed for each target thickness is also of interest and will be included in a separate publication.

As shown in figure 4, independent of target material, a similar scaling of the maximum ion energy with target thickness is measured. The rate of increase in the maximum carbon ion energy with decreasing target thickness is very similar to that reported by Neely *et al* [14] for protons (for Al target thickness above 100 nm) for an order of magnitude lower intensity. The maximum ion energy increases by approximately a factor of 2 when the target thickness is decreased by two orders of magnitude from 10 to 0.1 μm in both the cases. As the target thickness is decreased from 10 to 0.1 μm, the ratio L/r_{L} changes from 8 to 0.08. In the former case, transverse spreading of the fast electron population as it propagates within the target from the front to the rear surface is important in defining the maximum energy of TNSA ions, whereas for the latter case the electrons do not spread over an area much larger than the laser focal spot during their first transit of the target. In the case of targets for which $L \ll c\tau_{\mathrm{L}}/2$ (i.e. $\ll$7.5 μm), refluxing or recirculation [42] of electrons reflected in the sheath fields formed on both sides of the target is believed to occur, and Mackinnon *et al* [43] report that transient enhancements of the fast electron density due to recirculating electrons can increase the maximum energy of ions accelerated by TNSA.

To investigate the expected scaling of the maximum ion energy with the target thickness, L, we apply two analytical models: (i) the model presented by Schreiber *et al* [31] and (ii) the model described by Andreev *et al* for ultrahigh-contrast laser pulse interaction with thin target foils [32].

The model presented by Schreiber *et al* [31] is based on the surface charge set up by laser-accelerated electrons on the target rear surface and includes consideration of the radial extent of the charge cloud. The electron density is calculated assuming that the electrons are uniformly filling a circular region at the target rear surface with radius R. This radius is calculated assuming that the electrons are accelerated from the laser focal spot, with radius r_{L}, and transverse the target with thickness L in an angular cone with fixed half-angle θ_{e} (set equal to 20°), such that

$$R = r_L + L \cdot \tan\theta_{\mathrm{e}}. \tag{1}$$

The maximum observable ion energy $E_{\max}$ is determined from the expression

$$\frac{\tau_L}{\tau_0} = X\left(1 + \frac{1}{2}\frac{1}{1-X^2}\right) + \frac{1}{4}\ln\frac{1+X}{1-X}, \tag{2}$$

where $\tau_0 = R/v_\infty$ (v_∞ is the maximum possible ion velocity), $X = (E_{\max}/E_\infty)^{1/2}$ and

$$E_\infty = q_i 2 m_e c^2 (\eta P_L / P_R)^{1/2}, \tag{3}$$

where P_{L} is the laser power and $P_{\mathrm{R}} = 8.71$ GW is the relativistic power unit. q_{i} is the charge of the ion. η is the laser-to-fast electron energy conversion efficiency. Measurements of the laser energy reflected from the target (in the specular direction) indicate a total laser energy absorption of ∼30%. We therefore choose a realistic value of $\eta = 0.2$ for the total laser energy conversion to fast electrons in the calculation using the Schreiber *et al* model.

The Andreev *et al* [32] model, by contrast, is based on a self-consistent solution of the Poisson equation for the electric field responsible for ion acceleration and the equation of motion for the ion front. The model presented in [32] uses a rectangular density profile of the target, which is made up of two layers; the bulk of the target and a thin contaminant layer. The fast electron temperature and laser absorption are assumed to be dependent on the target thickness. The model has been calibrated against numerical simulations for angle of incidence equal to 45° [32]. The maximum observed ion energy, $E_{\max}$, is determined (in cgs units) by

$$E_{\max} \approx \frac{2.4 Z e E_\delta^+ r_{\mathrm{De}}}{\sqrt{1 + (L/r_{\mathrm{De}})^2}} + \frac{2 Z e E_{\mathrm{inf}}^+ r_{\mathrm{De}}}{\sqrt{1 + (r_{\mathrm{De}}/L)^2}}, \tag{4}$$

where $r_{\mathrm{De}} = \sqrt{T_{\mathrm{e0}}/4\pi e^2 n_{\mathrm{e0}}}$ is the Debye radius of hot electrons, Z is the atomic number of the target bulk or contaminant layer, e is the electronic charge and n_{e0} is the fast electron number density. $T_{e0}(L,\eta)$ is the fast electron temperature and is a function of the target thickness and the fraction of laser energy absorbed into the fast electrons. The electric fields associated with the ion front are $E_\delta^+ = 2\pi \mathrm{e}(Z_{\mathrm{b}} n_{\mathrm{ib}} L + Z_{\mathrm{c}} n_{\mathrm{ic}} L_{\mathrm{c}})$ and $E_{\mathrm{inf}}^+ = \sqrt{4\pi Z_{\mathrm{b}} n_{\mathrm{ib}} T_{\mathrm{e0}}}(\sqrt{2}/3^{3/4})(Z_{\mathrm{b}} n_{\mathrm{ib}}/n_{\mathrm{e0}}) + 2\pi e Z_{\mathrm{c}} n_{\mathrm{ic}} L_{\mathrm{c}}$ where subscripts b and c denote the target bulk and contaminant layers, respectively, and n_{i} denotes the ion density. The model is described in detail by Andreev *et al* [32]. For the calculations shown in figure 4 the target is assumed to be carbon with a 5 nm contaminant layer of hydrogen. The thickness of the carbon is varied.

Generally both models predict increasing ion energy with decreasing target thickness down to 100 nm, in qualitative agreement with the experimental measurements. An important difference in the models is that whilst the Schreiber *et al* model results in a saturation of the maximum ion energy as the sheath radius approaches the size of the laser focal spot, the model by Andreev *et al* predicts an optimum target thickness of ∼80 nm for the parameters of the experiment. This is higher than that predicted by the scaling laws presented by

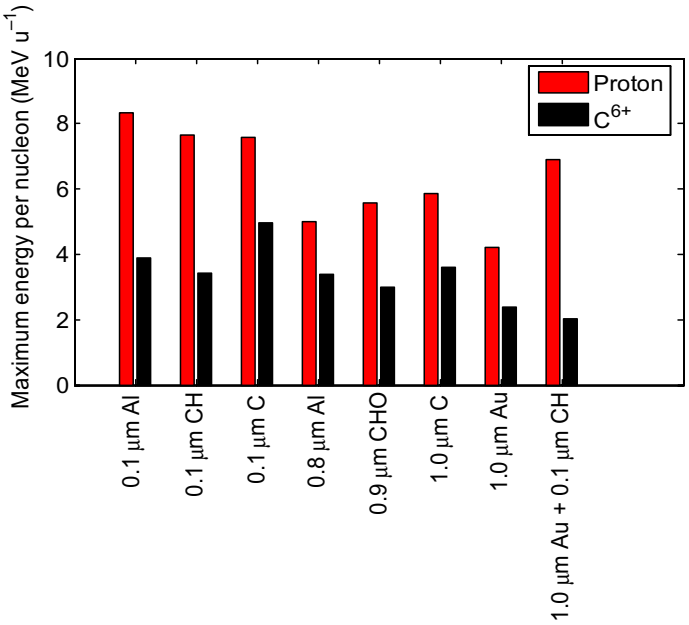

Figure 5. Maximum proton and C^{6+} ion energies (averaged over several shots on each target type) for given target compositions and thicknesses.

Esirkepov *et al* [20], which suggest an optimum thickness of ~20 nm for the laser parameters used. Experimentally, we observe a slight decrease in the average of the measured maximum C^{6+} ion energies obtained with 50 nm Al and C targets compared to the corresponding results for the 100 nm-thick targets (for $\theta_L = 0^\circ$), as shown in figure 4. However, as discussed above, due to the fact that we observe changes to the ion energy spectra with targets thinner than 50 nm, indicative of a transition away from the purely TNSA mechanism, we cannot conclusively state whether there is an optimum thickness for TNSA for the laser pulse parameters investigated. The results suggest that in terms of optimizing the acceleration of carbon ions, the thinnest foils enabled by the laser prepulse conditions down to ~100 nm should be used.

6. The effects of target composition

To investigate the extent to which the material properties and composition of the target influence the laser energy transfer to carbon ions, we irradiate a range of targets containing carbon, either in the bulk material of the target (i.e. C, CH and CHO), as an uncontrolled surface contamination layer (on Al and Au metallic foils) or as part of a controlled deposited layer on the target rear surface (Au–CH). This target composition scan is performed at $\theta_L = 35^\circ$. The results for the maximum proton and C^{6+} energies (averaged over 3–4 shots typically) are shown in figure 5 for $L = 0.1\ \mu$m and $L \sim 1\ \mu$m (0.8–1.1 μm).

We start by comparing proton and C^{6+} ion acceleration from the relatively low-density 'uniform' targets C, CH and CHO. The maximum proton energy does not differ significantly for these targets for a given L. However, the C^{6+} energy is highest for C targets. The presence of hydrogen in the composition of the target (in addition to the contamination layer) clearly produces a screening effect on the C^{6+} ion acceleration [36].

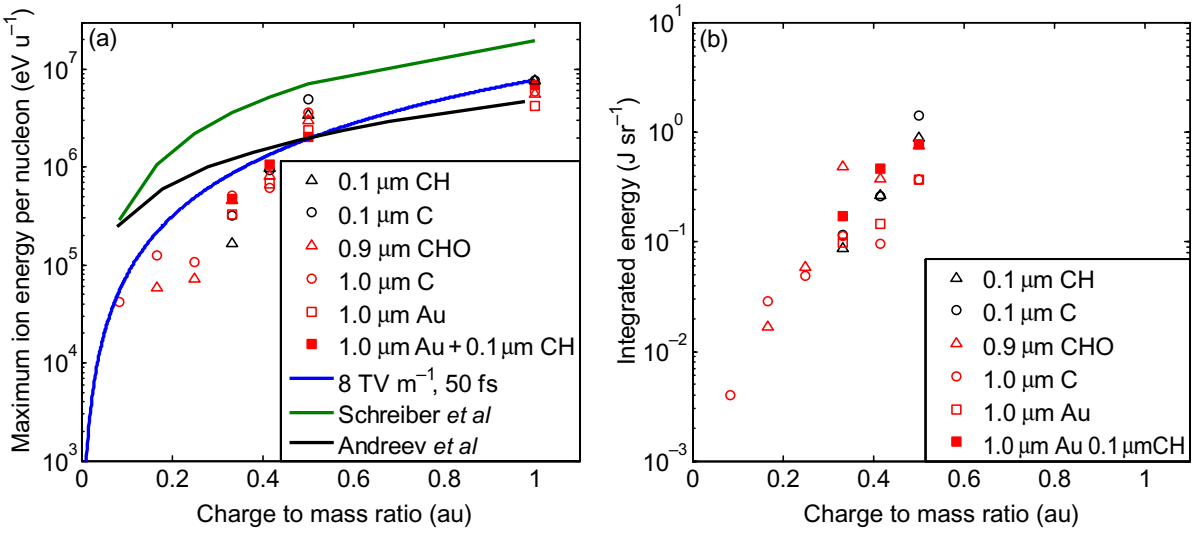

Figure 6. (a) Maximum ion energy and (b) total integrated ion energy as a function of the ion charge-to-mass ratio. The experimental data points are averages over several laser shots. Lines correspond to predictions using the analytical models of Schreiber *et al* [31] (green line) and Andreev *et al* [32] (black line). A simple calculation of the maximum ion energy obtained in an electric field of magnitude 8 TV m^{-1} for 50 fs (blue line), as described in the main text, is also included.

For the higher-density Al and Au targets, for which the TNSA protons and carbon ions are sourced only from hydrocarbon contamination layers on the target rear surface, a decrease in the maximum energies of both ion species is measured, particularly for the Au target. This is probably caused by the smaller number of those ions in the region of the acceleration field. The effect of adding a controlled 'source' layer (CH) of carbon and hydrogen to the target rear surface is also shown in figure 5. The availability of more hydrogen atoms in the region of the field enhances the acceleration of protons, producing a significant increase (from 4 to 7 MeV) in the averages of the measured maximum proton energies. A small decrease, however, is measured in the maximum carbon energy. These results further demonstrate that the presence of protons limits the maximum energies achievable for heavier ion species due to the screening of the acceleration field.

We conclude that for a given target thickness, carbon ion energies are maximized using a uniform C target and that proton energies are maximized by the use of a hydrogen-containing source layer on the rear surface of a high-Z target. However, this target produces the lowest-energy carbon ions due to proton screening of the acceleration field.

7. Ion charge state distributions

Figure 6 shows the measured *maximum* and *total* energies, averaged over several shots, of each ion species as a function of ion charge-to-mass ratio (q/m) for the targets discussed in the above section. Despite the differing target thicknesses, materials and compositions, clear trends are observed. An increase of about 2 orders of magnitude in both the maximum ion energy and total ion energy is measured over the range $q/m = 0.1$–0.5. These two parameters

are clearly strongly correlated. In most cases, increased energy coupling efficiency into a particular ion species results in an increase in ion number across the full energy spectrum, with a corresponding increase in the maximum ion energy detected.

Also shown in figure 6 are calculations of the maximum C^{q+}, $q = 1$–6, and proton energy scaling with q/m using the Schreiber *et al* [31] and Andreev *et al* [32] models as discussed above. The model calculations assume that all ions are created at the target rear surface. The initial charge state population, which has been shown to affect the energy scaling with ion q/m [36], is not considered. Nonetheless, the Schreiber *et al* model is found to reproduce the measured scaling very well, albeit the predicted energies are higher than measured for irradiation at 35° angle of incidence. The energies predicted by the Andreev *et al* model are closer to the experimental measurements. Both models predict higher energies for low-charge carbon ions than measured, and this is likely caused by additional shielding effects that are not accounted for in the models.

Finally, for comparison, the results of a simple calculation, in which it is assumed that all ion species are subjected to the same electrostatic field of magnitude 8 TV m^{-1} for 50 fs ($=\tau_L$), are also plotted. In this calculation, the magnitude of the electric field is a free parameter that is chosen by fitting to the measurements. At the rear surface of the target, ions can be produced by either collisional ionization or field ionization by barrier suppression mechanisms. Assuming field ionization to be the dominant ionization mechanism [3, 44], the minimum threshold field $E_q^{\text{Thres.}}$ for the production of an ion of charge q is calculated using

$$E_q^{\text{Thres.}} = U_{q-1}^2 \varepsilon_0 \pi / q\, e, \tag{5}$$

where U_q is the ionization potential in eV. $E_q^{\text{Thres.}} = 7$ TV m^{-1} for C^{6+} ions, which are efficiently produced in all of the laser shots considered. An electric field magnitude equal to 8 TV m^{-1} is therefore consistent with the ionization states measured. Despite the simplicity of this model, it reproduces the measured q/m scaling over most of the range, as shown in figure 6(a). The departure observed for low q/m ions is likely to result from a screening of the acceleration field acting on these ions by the acceleration of ions with larger q/m, as discussed in detail in [36]. We note that charge transfer can occur as the ions propagate from the source to the detector and that this can influence the charge state distribution measured. However, we do not expect this to have a strong influence as it would result in ions with different charge states with the same maximum energy, which is not observed in the experiment.

8. Summary

In summary, we report on an experimental investigation of the optimization of carbon ion acceleration driven by ultrahigh-contrast (10^{10}), ultrashort (50 fs) laser pulses focused to an average intensity equal to 7×10^{20} W cm^{-2}—about an order of magnitude higher intensity than previous ion acceleration experiments using laser pulses with tens of femtoseconds duration.

A number of conclusions are derived from our investigations of the TNSA-dominated regime.

1. Significantly higher (a factor of between 1.5 and 2) laser energy transfer to ions is obtained for irradiation at normal incidence compared to oblique incidence at 35° (with respect to the target normal). This result is supported by 1D-boosted PIC simulations, which show similar enhancement factors in the maximum ion energies. The simulations reveal that

the difference is due to higher-energy fast electrons produced for normal incidence. This result indicates that at ultrahigh intensities the p-component of the laser electric field has a reduced role in energy absorption, contrasting sharply with measurements made at lower intensities (5×10^{18} W cm^{-2}) [15], and that new absorption processes may be accessed at the ultrahigh intensity, ultrashort pulse regime explored.

2. The maximum energy of ions accelerated by TNSA increases with decreasing target thickness down to a thickness of ~100 nm for Al and C targets. For thinner targets, changes to the ion energy spectra suggest that the ion acceleration mechanism is not purely TNSA for the laser pulse parameters of the experiment.
3. The highest energy carbon ions at $\theta_L = 35^\circ$ are obtained with uniform carbon targets and the presence of hydrogen, either distributed throughout the target or as a layer on the rear surface, reduces the energy coupling efficiency to carbon ions. We note that removing the hydrogen-containing contamination layer from the target rear surface has been shown previously to increase the energy coupling efficiency to ions heavier than protons [3], [45–47]. By contrast, a high-Z target with a hydrogen source layer on the rear surface is best for optimizing proton acceleration.
4. There is a strong correlation between the measured *maximum* and *total* integrated ion energies and the scaling with q/m can be approximated to first order by assuming all ions are subjected to a constant electric field for the duration of the laser pulse. Departures from the model for low q/m ions suggest partial screening of the electric field acting on these ions by higher q/m species.

Acknowledgments

We acknowledge expert support of the staff at the Central Laser Facility. This work was supported by the UK Engineering and Physical Sciences Research Council (grant numbers EP/E035728/1 and EP/E048668/1) and the LIBRA consortium. APLR is grateful for the use of resources provided by STFC's e-Science facility.

References

[1] Clark E L *et al* 2000 Measurements of energetic proton transport through magnetized plasma from intense laser interactions with solids *Phys. Rev. Lett.* **84** 670–3

[2] Snavely R A *et al* 2000 Intense high-energy proton beams from petawatt-laser irradiation of solids *Phys. Rev. Lett.* **85** 2945–8

[3] Hegelich M *et al* 2002 MeV ion jets from short-pulse-laser interaction with thin foils *Phys. Rev. Lett.* **89** 085002

[4] Borghesi M, Fuchs J, Bulanov S V, MacKinnon A J, Patel P K and Roth M 2006 Fast ion generation by high-intensity laser irradiation of solid targets and applications *Fusion Sci. Technol.* **49** 412–439

[5] Cowan T *et al* 2004 Ultralow emittance, multi-MeV proton beams from a laser virtual-cathode plasma accelerator *Phys. Rev. Lett.* **92** 204801

[6] Roth M *et al* 2001 Fast ignition by intense laser-accelerated proton beams *Phys. Rev. Lett.* **86** 436–9

[7] Borghesi M, Schiavi A, Campbell D H, Haines M G, Willi O, MacKinnon A J, Gizzi L A, Galimberti M, Clarke R J and Ruhl H 2001 Proton imaging: a diagnostic for inertial confinement fusion/fast ignitor studies *Plasma Phys. Control. Fusion* **43** A267–76

[8] Ledingham K W D, McKenna P and Singhal R P 2003 Applications for nuclear phenomena generated by ultra-intense lasers *Science* **300** 1107–11
[9] McKenna P *et al* 2003 Demonstration of fusion-evaporation and direct-interaction nuclear reactions using high-intensity laser–plasma-accelerated ion beams *Phys. Rev. Lett.* **91** 075006
[10] Bulanov S V, Esirkepov T Z, Khoroshkov V S, Kuznetsov A V and Pegoraro F 2002 Oncological hadrontherapy with laser ion accelerators *Phys. Lett.* A **299** 240–7
[11] Murakami M *et al* 2008 Radiotherapy using a laser proton accelerator *Laser Driven Relativistic Plasmas Applied for Science, Industry, and Medicine. AIP Conf. Proc.* **1024** 275–300
[12] Malka V *et al* 2004 Practicability of protontherapy using compact laser systems *Med. Phys.* **31** 1587–92
[13] Ledingham K W D, Galster W and Sauerbrey R 2007 Laser-driven proton oncology—a unique new cancer therapy? *Br. J. Radiol.* **80** 855–8
[14] Neely D, Foster P, Robinson A, Lindau F, Lundh O, Persson A, Wahlström C-G and McKenna P 2006 Enhanced proton beams from ultrathin targets driven by high contrast laser pulses *Appl. Phys. Lett.* **89** 021502
[15] Ceccotti T, Lévy A, Popescu H, Réau F, D'Oliveira P, Monot P, Geindre J P, Lefebvre E and Martin Ph 2007 Proton acceleration with high-intensity ultrahigh-contrast laser pulses *Phys. Rev. Lett.* **99** 185002
[16] Henig A *et al* 2009 Enhanced laser-driven ion acceleration in the relativistic transparency regime *Phys. Rev. Lett.* **103** 045002
[17] Henig A *et al* 2009 Radiation-pressure acceleration of ion beams driven by circularly polarized laser pulses *Phys. Rev. Lett.* **103** 245003
[18] Lindau F, Lundh O, Persson A, McKenna P, Osvay K, Batani D and Wahlström C-G 2005 Laser-accelerated protons with energy-dependent beam direction *Phys. Rev. Lett.* **95** 175002
[19] McKenna P, Lindau F, Lundh O, Neely D, Persson A and Wahlström C-G 2006 High-intensity laser-driven proton acceleration: influence of pulse contrast *Phil. Trans. R. Soc.* A **364** 711–23
[20] Esirkepov T, Yamagiwa M and Tajima T 2006 Laser ion-acceleration scaling laws seen in multiparametric particle-in-cell simulations *Phys. Rev. Lett.* **96** 105001
[21] Yin L, Albright B J, Hegelich B M, Bowers K J, Flippo K A, Kwan T J T and Fernandez J C 2007 Monoenergetic and GeV ion acceleration from the laser breakout afterburner using ultrathin targets *Phys. Plasmas* **14** 056706
[22] Zhang X, Shen B, Li X, Jin Z, Wang F and Wen M 2007 Efficient GeV ion generation by ultraintense circularly polarized laser pulse *Phys. Plasmas* **14** 123108
[23] Robinson A P L, Zepf M, Kar S, Evans R G and Bellei C 2008 Radiation pressure acceleration of thin foils with circularly polarized laser pulses *New J. Phys.* **10** 013021
[24] Liseykina T V, Borghesi M, Macchi A and Tuveri S 2008 Radiation pressure acceleration by ultraintense laser pulses *Plasma Phys. Control. Fusion* **50** 124033
[25] Macchi A, Veghini S and Pegoraro F 2009 'Light Sail' acceleration reexamined *Phys. Rev. Lett.* **103** 085003
[26] Robinson A P L, Gibbon P, Zepf M, Kar S, Evans R G and Bellei C 2009 Relativistically correct hole-boring and ion acceleration by circularly polarized laser pulses *Plasma Phys. Control. Fusion* **51** 024004
[27] Macchi A, Liseikina T V, Tuveri S and Veghini S 2009 Theory and simulation of ion acceleration with circularly polarized laser pulses *C. R. Phys.* **10** 207–15
[28] Qiao B, Zepf M, Borghesi M and Geissler M 2009 Stable GeV ion-beam acceleration from thin foils by circularly polarized laser pulses *Phys. Rev. Lett.* **102** 145002
[29] Esirkepov T Z, Borghesi M, Bulanov S V, Mourou G and Tajima T 2004 Highly efficient relativistic-ion generation in the laser-piston regime *Phys. Rev. Lett.* **92** 175003
[30] Robson L *et al* 2007 Scaling of proton acceleration driven by petawatt-laser–plasma interactions *Nat. Phys.* **3** 58–62
[31] Schreiber J *et al* 2006 Analytical model for ion acceleration by high-intensity laser pulses *Phys. Rev. Lett.* **97** 045005

[32] Andreev A, Levy A, Ceccotti T, Thaury C, Platonov K, Loch R A and Martin Ph 2008 Fast-ion energy-flux enhancement from ultrathin foils irradiated by intense and high-contrast short laser pulses *Phys. Rev. Lett.* **101** 155002

[33] Andreev A A, Steinke S, Sokollik T, Schnürer M and Ter Avetsiyan S 2009 Optimal ion acceleration from ultrathin foils irradiated by a profiled laser pulse of relativistic intensity *Phys. Plasmas* **16** 013103

[34] Yin L, Albright B J, Hegelich B M and Fernández J C 2006 GeV laser ion acceleration from ultrathin targets: the laser break-out afterburner *Laser Part. Beams* **24** 291–8

[35] Bulanov S S *et al* 2008 Accelerating monoenergetic protons from ultrathin foils by flat-top laser pulses in the directed-Coulomb-explosion regime *Phys. Rev.* E **78** 026412

[36] McKenna P *et al* 2007 Low- and medium-mass ion acceleration driven by petawatt laser–plasma interactions *Plasma Phys. Control. Fusion* **49** B223–31

[37] Brunel F 1987 Not-so-resonant, resonant absorption *Phys. Rev. Lett.* **59** 52–5

[38] Gibbon P 1994 Efficient production of fast electrons from femtosecond laser interaction with solid targets *Phys. Rev. Lett.* **73** 664–7

[39] Robinson A P L, Neely D, McKenna P and Evans R G 2007 Spectral control in proton acceleration with multiple laser pulses *Plasma Phys. Control. Fusion* **49** 373–84

[40] Gibbon P, Andreev A, Lefebvre E B, Ruhl H, Delettrez J and Bell A R 1999 Calibration of one-dimensional boosted kinetic codes for modeling high-intensity laser–solid interactions *Phys. Plasmas* **6** 947–53

[41] Bourdier A 1983 Oblique incidence of a strong electromagnetic wave on a cold inhomogeneous electron plasma. Relativistic effects *Phys. Fluids* **26** 1804–7

[42] Sentoku Y, Cowan T E, Kemp A and Ruhl H 2003 High energy proton acceleration in interaction of short laser pulse with dense plasma target *Phys. Plasmas* **10** 2009–15

[43] Mackinnon A J, Sentoku Y, Patel P K, Price D W, Hatchett S, Key M H, Andersen C, Snavely R and Freeman R R 2002 Enhancement of proton acceleration by hot-electron recirculation in thin foils irradiated by ultraintense laser pulses *Phys. Rev. Lett.* **88** 215006

[44] McKenna P *et al* 2007 Lateral electron transport in high-intensity laser-irradiated foils diagnosed by ion emission *Phys. Rev. Lett.* **98** 145001

[45] McKenna P *et al* 2004 Characterization of proton and heavier ion acceleration in ultrahigh-intensity laser interactions with heated target foils *Phys. Rev.* E **70** 036405

[46] Hegelich B M *et al* 2005 Spectral properties of laser-accelerated mid- Z MeV/u ion beams *Phys. Plasmas* **12** 056314

[47] Hegelich B M, Albright B J, Cobble J, Flippo K, Letzring S, Paffett M, Ruhl H, Schreiber J, Schulze R K and Fernandez J C 2006 Laser acceleration of quasi-monoenergetic MeV ion beams *Nature* **439** 441–4